Understanding the role of water evaporation and condensation in applied smoldering systems

Jiahao Wang [a, *], Marco A. B. Zanoni [a], José L. Torero [b], Jason I. Gerhard [a, ‡]

[a] Department of Civil and Environmental Engineering, The University of Western Ontario, London, Ontario, N6A 5B9, Canada

[b] Department of Civil, Environmental and Geomatic Engineering, University College London, London, WC1E 6BT, UK

* Corresponding author at Department of Civil and Environmental Engineering, The University of Western Ontario, Claudette Mackay-Lassonde Pavilion, Rm. 1317, London, Ontario, Canada N6A 5B9. E-mail address: jwan753@uwo.ca (Jiahao Wang).

‡ Deceased

Abstract

Accurately resolving the way energy is stored and transferred is critical to applied smoldering systems in porous media. Water evaporation and condensation are important mechanisms in the energy conservation of smoldering. This is particularly important when significant water presence can affect the potential for self-sustained smoldering as it occurs in a broad range of practical applications. This paper describes a one-dimensional smoldering model considering water phase change. The model was calibrated to a series of wet smoldering experiments of GAC varying water saturation from 5% to 20%. The results show that introducing simple calibration constants on the thermal properties of a wet porous medium can accurately predict the transient and spatial resolution of the progression of evaporation, condensation, and smoldering reactions. A sensitivity analysis suggests that wet smoldering could be improved by increasing fuel concentration and injected air flux, which provides practical insights into wet smoldering applications. In addition, the model was applied to establish five characteristic zones for the wet smoldering front: pre-heating, evaporation, smoldering, cooling and condensation. The evaporation and condensation zones challenge smoldering propagation due to the high water saturation. The pre-heating zone represents the region separating the smoldering front and evaporation zone, which serves as an important dry buffer and requires a minimum thickness (4 mm) to avoid extinction.

Keywords: Smoldering combustion; Water phase change; Evaporation; Condensation; Energy and mass balance

Nomenclature

Latin Letters

A	Pre-exponential factor, s^{-1}
A_s	Surface area, m^2
A_{cs}	Cross-section area, m^2
C_p	Specific heat capacity, J kg^{-1} K^{-1}
d_p	Particle diameter, mm
D_g	Gas diffusion coefficient, m^2 s^{-1}
E	Activation energy, kJ mol^{-1}
$\dot{E}$	Energy rate, J s^{-1}
h_{sg}	Interfacial heat transfer coefficient, W m^{-2} K^{-1}
k	Thermal conductivity, W m^{-1} K^{-1}
k_{evap}	Equilibrium time constant, s^{-1}
k_p	Intrinsic permeability, m^2
L	Contaminated bed height, m
m	Mass, kg
$\dot{m}$	Mass flow, kg s^{-1}
$\dot{m}_w'''$	Evaporation rate, kg m^{-3} s^{-1}
M	Molar weight, g mol^{-1}
Nu	Nusselt number
P	Pressure, Pa
Pr	Prandtl number
$\dot{q}''$	Heat Flux, W m^{-2}
r	Column radius, m
R	Ideal gas constant, J K^{-1} mol^{-1}
Re	Reynolds number
R_{GAC}	Reaction rate, s^{-1}
S	Saturation
T	Temperature, K
u	Velocity, m s^{-1}

U	Global heat loss coefficient, W m^{-2} K^{-1}
V	Volume, m^3
v_{O2}	Oxygen stoichiometric coefficient, $kg.O_2$ $kg.fuel^{-1}$
X	Molar fraction
Y	Mass fraction

Greek Symbols

ΔH_{evap}	Heat of evaporation, J kg^{-1}
ΔH_{GAC}	Heat of oxidation, MJ kg^{-1}
δ	Thickness, cm
ρ	Density, kg m^{-3}
ϕ	Porosity
σ	Stefan–Boltzmann constant, W m^{-2} K^{-4}
μ	Dynamic viscosity, Pa.s
δ, γ	Empirical constant

Subscripts/Superscript

a	Air
avg	Average
b	Bulk
Cl	Cylinder
cond	Conduction
conv	Convection
eff	Effective
evap	Evaporation
exp	Experiment
f	Final
g	Gas
h	Heater
in	Inlet
N	Normalized

num	Numerical
0	Ambient/Initial
Out	Outlet
p	Peak
pre	Pre-heating
r	Residual
rad	Radiation
s	Solid/sand/smoldering
sp	Sphere
stab	Stable
v	Vapor
w	Water

1 Introduction

Smoldering is a part of terrestrial ecosystems, naturally occurring in porous solid fuels, e.g., peat and coal [1]. It has been recently engineered as an effective thermal system for environmentally-beneficial and waste-to-energy purposes, including remediating contaminated sites and addressing waste challenges. To date, applied smoldering has undergone numerous successful laboratory and pilot tests for treating organic wastes, such as sewage sludge [2-6], feces [7-10], anaerobic digestate [11], food waste [12] and oil sludge [13-14]. Most of the above wastes had moisture content (MC) above 50 wt.%, which suggests the potential of applied smoldering to efficiently destruct high moisture content wastes (HMWs).

Smoldering is driven by an oxidation reaction occurring on the surface of the condensed-phase fuel. It involves heterogeneous reactions and the multi-phase transport of mass, momentum, and energy [15]. The transport of energy has been successfully simulated in many studies aiming to predict the smoldering performance as a treatment technology [16-25]. Once the exothermic oxidation generates sufficient energy to overcome heat losses (i.e., a positive energy balance), smoldering has the potential to be self-sustained and can propagate without external energy input.

In the applied smoldering of HMWs, MC acts as an energy sink, in which a high MC can significantly impact reaction propagation and lead toward extinction. A limiting initial MC, preventing smoldering from being self-sustained, is often discussed for treating HMWs and the suppression of peat fires. Sewage sludge and feces can be successfully smoldered with a MC up to 75-80 wt.% [2, 7, 26], whereas raw food waste and organic substrate can be disposed via smoldering with 40 wt.% [12] and 82 wt.% [11] MC, respectively. Additionally, Rein et al. [27] and Prat-Guitart et al. [28] showed that the smoldering of peat can be self-sustained up to 55-60

wt.% MC. Although a specified initial MC is defined as the limiting condition, both smoldering front and MC will evolve in space and time. In the above studies, the dynamic MC changes, and their interaction with the evolving smoldering front are not well understood.

Yermán et al. [7] observed an increase in MC along the upward forward smoldering reactor, suggesting that the water vapor condenses ahead of the smoldering reaction due to low temperatures. This liquid re-condensation is significant in long reactors [29] and continuous operations, which might lead to a higher MC (i.e., critical MC) than the initial condition, causing weak smoldering or extinction [15]. Therefore, smoldering in the presence of water (wet smoldering) is complex and involves coupled mechanisms such as water phase change, heat and mass transfer in porous media and smoldering reactions [30]. An accurate numerical investigation is required for the fundamental understanding of wet smoldering and the development of full-scale applied smoldering systems for treating HMWs.

Few studies have developed numerical models to predict wet smoldering processes. Most of them investigated in the context of peat fire, which typically treats water evaporation as a heat sink governed by an Arrhenius chemical reaction [31-39]. This approach is valuable in understanding the impact of endothermic evaporation on limiting the smoldering process; and it is practical for the natural open system (e.g., lateral spread of peat fire) and reactive porous media (e.g., peat), in which water is evaporating to the atmosphere rapidly. Nevertheless, under most practical applications of smoldering, the conditions are not favorable for this modelling approach. The chemical reaction treatment simplifies water movement, ignoring water phase changes and mass transfer between phases in the smoldering system, which results in an incomplete consideration of the global energy balance [1]. Furthermore, water condensation has not been explored in such models; consequently, it may not be appropriate in evaluating the fate of wet smoldering in a closed

system or inert porous media (e.g., sand), i.e., applied smoldering where vapor re-condensation exists [7]. In particular, when the reaction is close to extinction.

Accurately resolving the energy balance is critical to smoldering applications as it affects peak temperatures and front velocities required for the contaminant destruction [2, 40-43], resource recovery [44] and energy efficiency [17-19, 21-23, 45-46]. Therefore, to simulate the smoldering of HMWs, water evaporation and condensation must be integrated as a phase-change process in the porous system. To the author's knowledge, only a theoretical study with no experimental validation explored water evaporation and condensation in filtration combustion, where water evaporation and condensation fronts were travelling with a constant velocity ahead of smoldering front [47].

Recently, Zanoni et al. [48] developed a one-dimensional (1-D) multiphase model of water evaporation and condensation in a high-temperature (500 °C) inert porous medium. The model revealed that Local Thermal Non-Equilibrium (LTNE) needs to be assumed in high-temperature drying processes, and the thermal properties of the porous media were significantly affected by MC and temperature. Heat conduction primarily occurs through particle contact in dry porous media whereas air obstructs the heat conduction. However, the replacement of air with a more conductive medium (e.g., water) provides a significant improvement of heat conduction between sand particles in wet porous media [49], leading to a non-linear relationship between MC and thermal conductivity [50]. Besides, the relationship between heat capacity and temperature is also non-linear in the presence of water, which is affected by the water evaporation [51-52]. As both thermal conductivity and heat capacity are crucial for the global energy balance, a careful interpretation is required in simulating water evaporation in porous systems.

This work takes [48]'s approach to water evaporation and introduces an upward forward smoldering front propagation, thus delivering a tool for the characterization of wet smoldering. The wet smoldering model was calibrated to a series of smoldering experiments varying the initial water saturation of the porous medium. The model was then employed to quantify the dynamic phenomena resulting from the presence of water in the smoldering system, including global energy and mass balance, the structure of wet smoldering front, and the interaction between smoldering and evaporation front. Finally, the model was extrapolated for sensitivity analysis of the impact of key parameters on wet smoldering. Overall, this study provides novel and important insights into wet smoldering applications, allowing better management of treating HMWs as well as other related systems that involve similar processes, e.g., peat fires and enhanced oil recovery.

2 Methodology

2.1 Modelling

A 1-D wet smoldering model was developed in COMSOL with a 0.5 mm mesh size and a varied time-step to meet stability criteria. The computation domain represents the centerline of the packed bed ($H = 0.88$ m) as shown in the experimental setup in Fig. 1. The treatment layer was composed of water, sand, and granular activated carbon (GAC). GAC is a by-product of coal pyrolysis [53-54] and it was used as the surrogate fuel in previous smoldering studies. A proximate analysis revealed that GAC is composed mostly of fixed carbon (91.4%) with low volatile content (3.2%) [55]. Moreover, TGA/DSC experiments [23] showed no significant mass loss under nitrogen atmosphere. Therefore, pyrolysis reactions can be neglected and GAC smoldering can be modelled with a 1-step oxidation reaction [20, 22].

A set of smoldering scenarios was simulated to investigate the impact of initial water saturation ($S_{w,0}$, the ratio of water volume/pore volume), GAC concentration (C_f, the ratio of GAC mass/sand mass) and injected airflow ($u_{g,in}$) on wet smoldering (Table 1), where Cases #1, 4, 7-9 were compared to experimental tests. All cases were set up as an upward forward smoldering system as it is energy efficient, easy to be implemented and has been widely applied for environmentally-beneficial and waste-to-energy processes. Among these cases, a base case experiment (Exp. #4) was conducted in quadruplicate and another four experiments (Exp. #1, 7-9) varied $S_{w,0}$. The model considers the conservation of mass, momentum and energy, along with GAC smoldering reaction and water phase change, in which the treatment of smoldering is based on Zanoni et al. [20] and the moisture follows Zanoni et al. [48]. Table 1 summarizes the key operational parameters for all cases, including the time when airflow was injected (t_g) and heater was turned

off (t_h), calibrated numerical constants (δ, k_{evap}, γ), and the difference between experimental and numerical temperatures for Cases #1, 4, 7-9, which are detailed in Section 2.1.1.

Table 1: Summary of all cases

Case (-)	Exp. (-)	Num. [a] (-)	$S_{w,0}$ [b] (%)	C_f (%)	$u_{g,in}$ (cm/s)	t_g (s)	t_h (s)	δ/k_{evap} (s^{-1})	γ	Error (%)	SS [e]
1	1	√	5.0	3	5.0	3770	4440	6/0.5	1.000	6.19	SS
2	-	√	10.0	2	5.0	3815	4483	6/0.5	0.850	-	SS
3	-	√	10.0	3	3.3	3815	4483	6/0.5	0.850	-	SS
4	4	√	10.0	3	5.0	3815 ± 217 [c]	4483 ± 250 [c]	6/0.5	0.850	5.89	SS
5	-	√	10.0	3	6.7	3815	4483	6/0.5	0.850	-	SS
6	-	√	10.0	4	5.0	3815	4483	6/0.5	0.850	-	SS
7	1	√	12.5	3	5.0	4010	4835	6/0.5	0.829	8.51	SS
8	1	√	15.0	3	5.0	4740	5520	6/0.5	0.800	8.58	SS
9	1	√	20.0	3	5.0	6000	6480	6/0.5	0.780	17.31	SS
10	-	√	30.0	2	5.0	6000 [d]	6480 [d]	6/0.5	0.700	-	SS
11	-	√	30.0	3	3.3	6000	6480	6/0.5	0.700	-	SS
12	-	√	30.0	3	5.0	6000	6480	6/0.5	0.700	-	SS
13	-	√	30.0	3	6.7	6000	6480	6/0.5	0.700	-	SS
14	-	√	30.0	4	5.0	6000	6480	6/0.5	0.700	-	SS
15	-	√	40.0	3	5.0	6000	6480	6/0.5	0.667	-	SS

16	-	√	50.0	3	5.0	6000	6480	6/0.5	0.639	-	BSS
17	-	√	60.0	2	5.0	6000	6480	6/0.5	0.617	-	NSS
18	-	√	60.0	3	3.3	6000	6480	6/0.5	0.617	-	NSS
19	-	√	60.0	3	5.0	6000	6480	6/0.5	0.617	-	BSS
20	-	√	60.0	3	6.7	6000	6480	6/0.5	0.617	-	SS
21	-	√	60.0	4	5.0	6000	6480	6/0.5	0.617	-	SS
22	-	√	70.0	3	5.0	6000	6480	6/0.5	0.599	-	NSS
23	-	√	80.0	3	5.0	6000	6480	6/0.5	0.584	-	NSS

[a] check mark stands for simulation performed

[b] $\emptyset = 0.41$

[c] 95% confidence interval

[d] Cases #10-23: t_g and t_h follow Case #9

[e] SS: self-sustained; NSS: non-self-sustained; BSS: borderline-self-sustained

2.1.1 Governing Equations

The kinetics for GAC smoldering assumes a first-order Arrhenius reaction without pyrolysis [23]:

$$GAC + v_{O_2} \xrightarrow{R_{GAC}} Gas \tag{1}$$

$$R_{GAC} = A_{GAC} exp\left(-\frac{E_{GAC}}{RT_s}\right)(Y_{GAC})(Y_{O_2}) \tag{2}$$

The conservation of mass for solid is:

$$\frac{\partial(Y_{GAC})}{\partial t} = -R_{GAC} \tag{3}$$

where Y_{GAC} is defined as $Y_{GAC} = m_{GAC}/m_{GAC,0}$.

The conservation of mass for liquid is:

$$\phi\rho_w \frac{\partial(S_w)}{\partial t} = -\dot{m}_w''' \tag{4}$$

Water is assumed to be immobile, chemically inert and only becomes vapor with the evaporation rate ($\dot{m}_w'''$) described by Eq. 24 [47-48]. The porosity (ϕ) of porous media is defined as the volume fraction of total pore space, which is occupied by gas ($\phi_g = \phi S_g$), liquid ($\phi_w = \phi S_w$) and GAC ($\phi_{GAC} = \phi S_{GAC}$). $\phi_{GAC} = (\rho_{GAC,b} Y_{GAC})/\rho_{GAC}$. Therefore, $\phi_g + \phi_w + \phi_{GAC} = \phi$ and $S_g + S_w + S_{GAC} = 1$.

The conservation of mass for total gas, vapor included is:

$$\frac{\partial(\phi S_g \rho_g)}{\partial t} + \frac{\partial(\rho_g u_g)}{\partial x} = \rho_{GAC,b} R_{GAC} + \dot{m}_w''' \tag{5}$$

where ρ_g is determined by Eq. 10, and water vapor and air have the same velocity, u_g [56-58]:

$$u_g = -\frac{k_p}{\mu_g}\frac{\partial P_g}{\partial x} \tag{6}$$

P_g follows Dalton's law, $P_g = P_a + P_v$ [59] and μ_g is defined by the weighted average:

$$\mu_g = \mu_a(1 - Y_v) + \mu_v(Y_v) \tag{7}$$

where Y_v is the mass fraction of water vapor:

$$\frac{\partial(\phi S_g \rho_g Y_v)}{\partial t} + \frac{\partial(\rho_g u_g Y_v)}{\partial x} = \frac{\partial}{\partial x}\left(\phi S_g \rho_g D_{g,wv} \frac{\partial Y_v}{\partial x}\right) + \dot{m}_w''' \tag{8}$$

The conservation of mass for the bulk transport of oxygen is:

$$\phi \frac{\partial(\rho_g S_g Y_a Y_{O_2})}{\partial t} + \frac{\partial(\rho_g u_g Y_a Y_{O_2})}{\partial x} = \phi \frac{\partial}{\partial x}\left(\rho_g S_g Y_a D_{g,O_2} \frac{\partial Y_{O_2}}{\partial x}\right) - \rho_{GAC,b} v_{O_2} R_{GAC} \tag{9}$$

The total gas density (ρ_g) follows the ideal gas law:

$$\rho_g = \frac{P_g M_g}{R T_g} \tag{10}$$

where:

$$M_g = X_v M_v + (1 - X_v)(M_a) \tag{11}$$

$$X_v = \frac{Y_v M_a}{Y_v M_a + (1 - Y_v) M_v} \tag{12}$$

$$P_v = X_v P_g \tag{13}$$

$$P_a = (1 - X_v) P_g \tag{14}$$

The model solved the transient energy equation for solid and gas phases. Liquid and solid are assumed to be in Local Thermal Equilibrium (LTE) forming the "stationary" phase. This assumption is reasonable since MC is relatively low so that most of the water molecules are getting adsorbed to the sand particles, behaving as an immobile film coating the sand. However, Local Thermal Non-Equilibrium (LTNE) is applied between stationary and gas phases [60]:

$$\left(\rho C_p\right)_{eff}\frac{\partial T_s}{\partial t}=\frac{\partial}{\partial x}\left(k_{eff}\frac{\partial T_s}{\partial x}\right)-U\left(\frac{A_{s,cl}}{V_{cl}}\right)(T_s-T_0)+h_{sg}\left(\frac{A_{s,sp}}{V_{sp}}\right)\left(T_g-T_s\right)-\rho_{GAC,b}\Delta H_{GAC}R_{GAC}-\chi\Delta H_{evap}\dot{m}_w'''$$ (15)

$$\phi S_g\left(\rho_g C_{p_g}\right)\frac{\partial T_g}{\partial t}+\rho_g C_{p_g}u_g\frac{\partial T_g}{\partial x}=\phi S_g\frac{\partial}{\partial x}\left(k_g\frac{\partial T_g}{\partial x}\right)+h_{sg}\left(\frac{A_{s,sp}}{V_{sp}}\right)\left(T_s-T_g\right)+\dot{m}_w'''C_{p_v}(T_s-T_g)-(1-\chi)\Delta H_{evap}\dot{m}_w'''$$ (16)

The energy equations assume that both the volumetric energies of GAC oxidation ($\rho_{GAC,b}\Delta H_{GAC}R_{GAC}$) and water evaporation ($\Delta H_{evap}\dot{m}_w'''$) originally act on the stationary phase, except when T_s is below 20 ℃, the water evaporation term is switched into the gas phase during the evaporation ($\dot{m}_w''' > 0$) by setting χ from 1 to 0. Switching the evaporation source term between phases is to avoid numerical instability during high saturation conditions. Heat transfer between solid and gas phases is via an interfacial heat transfer term (h_{sg}) and an additional vapor mass transfer term, $\dot{m}_w'''C_{p_v}(T_s-T_g)$. Besides, a global heat loss coefficient (U), using the surface area per unit volume ratio ($A_{s,cl}/V_{cl}=2/r$), is included in Eq. 15 to calculate the system energy loss to the surrounding environment.

The heat of evaporation (ΔH_{evap}) is temperature-dependent, defined by [61]:

$$\Delta H_{\ evap}=2501.05\ x10^3\left(\frac{647.3-T_s}{643.3-273.15}\right)^{0.3298}$$ (17)

Eqs. 15-16 assume that the porous medium was homogeneous and sand particles were taken as spheres ($A_{s,sp}/V_{sp}=6(1-\phi)/d_p$). The interfacial heat transfer coefficient (h_{sg}) uses Eq.18 for smoldering conditions [60]:

$$Nu=\frac{h_{sg}d_p}{k_g}=0.001\left(Re^{1.97}Pr^{1/3}\right)$$ (18)

However, Eq. 18 requires forced air conditions ($Re > 0$). In the case of $Re = 0$, temperatures are relatively low, and energy transfer between solid and gas phases can be assumed to occur instantaneously, i.e., LTE exists [31, 34, 47-48]. Therefore, Eqs. 15-16 were set as LTE for $0 \leq t \leq t_g$, represented by a large h_{sg} (500 W m^{-2} K^{-1}), and then set as LTNE for $t_g < t \leq t_f$ following Eq. 18.

The effective "*eff*" in Eqs. 15-16 refers to the properties of the sand-liquid-GAC mixture in the stationary system. Zanoni et al. [48] found that additional empirical coefficients (δ, γ) needed to be included in the linear average determination of k_{eff} and $(\rho C_p)_{eff}$ to account for high thermal diffusivity in the presence of water [62]. It is due to the fact that water phase change occurs in a low-temperature range (≤ 100 ℃), therefore energy balance is sensitive to any heat transfer in the system. Consequently, the empirical coefficients δ and γ are applied to offset possible unknown heat transfer phenomena in the experiments that were not captured by the model, such as 2-D impact of the metal column wall, which are detailed in Section 3.1.

$$k_{eff} = \begin{matrix} \delta\,[(1-\phi)(k_s + k_{rad}) + (\phi S_w)k_w + \phi_{GAC}k_{GAC}] & (0 \leq t \leq t_g) \\ (1-\phi)(k_s + k_{rad}) + (\phi S_w)k_w + \phi_{GAC}k_{GAC} & (t_g < t \leq t_f) \end{matrix} \quad (19)$$

$$(\rho C_p)_{eff} = \gamma[(1-\phi)\rho_s C_{ps} + (\phi S_w)\rho_w C_{pw} + (\emptyset_{GAC})\rho_{GAC} C_{pGAC}] \quad (20)$$

$$C_{pg} = (1 - Y_v)C_{pa} + Y_v C_{pv} \quad (21)$$

$$k_g = (1 - Y_v)k_a + Y_v k_v \quad (22)$$

Radiation heat transfer ("*rad*") followed the Rosseland approximation and was expressed as a radiative conductivity, $k_{rad} = 16\sigma d_p T_s^3/3$ [60].

Empirical coefficients δ, γ and k_{evap} were calibrated to smoldering experiments for Cases #1, 4, 8-9 and then validated with Case #7 without any additional calibration. The model calibration involved minimizing the error between the numerical (*num*) and experimental temperature evolution (*exp*), giving equal weight to three aspects of the fit: average peak temperature (T_P), plots of temperature versus time when air is off (conductive heat transfer dominated, $T(t)_{avg\_cond}$), and when air is on (convective heat transfer dominated, $T(t)_{avg\_conv}$):

$$Error\ (\%) = \left(NRMSD_{T(t)_{avg\_cond}}/3 + NRMSD_{T(t)_{avg\_conv}}/3 + \left|\frac{T_{pexp} - T_{pnum}}{T_{pnum}}\right|/3\right) * 100 \qquad (23)$$

where the average Normalized Root-Mean-Square Deviation (NRMSD) follows the approach modified from Miry et al. [23] and Zanoni et al. [60].

The model parameters not described in the text are presented in Table 2 and the initial and boundary conditions are defined in Table 3. Note that the inlet boundary condition specifies a time-dependent heat flux $\dot{q}''_{in,t}$ until the cone heater reaches the stable temperature at t_{stab}, after which a constant flux ($\dot{q}''_{stab}$) is applied. Then a constant airflow ($u_{g,in}$) is initiated at the inlet boundary at t_g, and the cone heater is turned off at t_h.

Table 2: Model input parameters

Parameter	Value	Unit	Reference
$log(A_{GAC})$	3.79	$log(s^{-1})$	[23]
C_{pGAC}	1100	J kg^{-1} K^{-1}	[63]
C_{ps}	$2.49(T_s)+39.06$	J kg^{-1} K^{-1}	[58]
C_{pa}	$-3x10^{-5}(T_g^2)+0.2261(T_g)+940.35$	J kg^{-1} K^{-1}	[64]
C_{pv}	$7x10^{-5}((T_g-273.15)^2)+$ $0.5583(T_g-273.15)+1835.8$	J kg^{-1} K^{-1}	[64]
C_{pw}	$5.47x10^{-6}((T_s-273.15)^2)+$ $9.086x10^{-5}(T_s-273.15)+4.176$	J kg^{-1} K^{-1}	[65]
d_p	1.775	mm	Measured

$D_{g,wv}$	$8x10^{-5}$	$m^2\ s^{-1}$	[48]
D_{g,O_2}	$4.53x10^{-5}$	$m^2\ s^{-1}$	[66]
E_{GAC}	72.92	kJ mol^{-1}	[23]
ΔH_{GAC}	-24.9	MJ kg^{-1}	[23]
H	0.88	m	Measured
k_{GAC}	0.25	W $m^{-1}\ K^{-1}$	[63]
k_s	$0.000541(T_s)+0.1044$	W $m^{-1}\ K^{-1}$	[60]
k_a	$-1x10^{-8}(T_g^2)+8x10^{-5}(T_g)+4.3x10^{-3}$	W $m^{-1}\ K^{-1}$	[64]
k_v	$4x10^{-8}((T_g-273.15)^2)+$ $8x10^{-5}(T_g-273.15)+0.0152$	W $m^{-1}\ K^{-1}$	[64]
k_w	$6.7x10^{-5}((T_s-273.15)^2)+$ $1.76\ x10^{-3}(T_s-273.15)+0.571$	W $m^{-1}\ K^{-1}$	[65]
k_p	$5.0x10^{-10}$	m^2	Measured
L	0.73	m	This work
M_a	28.97	g kg^{-1}	[59]
M_v	18.01	g kg^{-1}	[59]
ϕ	0.41	-	Measured
ρ_{GAC}	1311	kg m^{-3}	[23]
$\rho_{GAC,b}$	42.89	kg m^{-3}	Measured
ρ_s	2650	kg m^{-3}	[60]
ρ_w	995.74	kg m^{-3}	[65]
$P_{g,0}$	1.0156	kPa	[48]
$\dot{q}''_{in,t}$	$9x10^{-8}(t^3)-\ 2x10^{-4}(t^2)+0.1263(t)-2.1887$	kW m^{-2}	Measured
$\dot{q}''_{stab}$	22.028	kW m^{-2}	[23]
r	0.054	m	Measured
R	8.314	J $K^{-1}\ mol^{-1}$	[59]
t_{stab}	450	s	Measured
t_f	24000	s	This work
T_0	293.15	K	This work
U	5.225	W $m^{-2}\ K^{-1}$	[23]
μ_a	$-9x10^{-12}(T_g^2)+4x10^{-8}\ (T_g)+6x10^{-6}$	Pa s	[64]
μ_v	$7x10^{-12}(T_g^2)+4x10^{-8}\ (T_g)+9x10^{-6}$	Pa s	[64]
v_{O_2}	2.304	kg O_2 kg $fuel^{-1}$	[23]
$Y_{v,0}$	0.00143	-	[48]
$Y_{O_2,0}$	0.23	-	[23]

Table 3: Initial and boundary conditions

Eq.	Initial conditions	Boundary conditions
3	$t = 0 \Longrightarrow Y_{GAC} = 1$	-
4	$t = 0 \Longrightarrow S_w = S_{w,0}$	-
5-6	$t = 0 \Longrightarrow P_g = P_{g,0}$	$x = 0 \Longrightarrow \rho_g u_g(t) \Longrightarrow \begin{cases} u_g(t) = 0 & \rightarrow 0 \leq t \leq t_g \\ u_g(t) = u_{g,in} & \rightarrow t_g < t \leq t_f \end{cases}$ $x = H \Longrightarrow P_g = P_{g,0}$
8	$t = 0 \Longrightarrow Y_v = Y_{v,0}$	$x = 0 \Longrightarrow Y_v = Y_{v,0}$ $x = H \Longrightarrow -\phi S_g \rho_g D_{g,wv} \frac{\partial (Y_v)}{\partial x} = \rho_g u_g \left(Y_{v,0} - Y_v\right)$
9	$t = 0 \Longrightarrow Y_{O_2} = Y_{O_2,0}$	$x = 0 \Longrightarrow Y_{O_2} = Y_{O_2,0}$ $x = H \Longrightarrow -\phi S_g \rho_g Y_a D_{g,O_2} \frac{\partial \left(Y_{O_2}\right)}{\partial x} = \rho_g u_g Y_a \left(Y_{O_2,0} - Y_{O_2}\right)$
15-16	$t = 0 \Longrightarrow T_s = T_g = T_0$	$x = 0 \Longrightarrow \begin{cases} -\left(k_{eff}\right) \frac{\partial T_s}{\partial x} = \dot{q}''_{in,t} & \rightarrow t_0 \leq t \leq t_{stab} \\ -\left(k_{eff}\right) \frac{\partial T_s}{\partial x} = \dot{q}''_{stab} & \rightarrow t_{stab} \leq t \leq t_h \\ -\left(k_{eff}\right) \frac{\partial T_s}{\partial x} = 0 & \rightarrow t_h < t \leq t_f \\ T_g = T_s & \rightarrow t_0 \leq t \leq t_g \\ T_g = T_0 & \rightarrow t_g < t \leq t_f \end{cases}$ $x = H \Longrightarrow \begin{cases} -\left(k_{eff}\right) \frac{\partial T_s}{\partial x} = 0 \\ -\left(k_g\right) \frac{\partial T_g}{\partial x} = 0 \end{cases}$

2.1.2 Water Phase Change

Water evaporation rate ($\dot{m}_w'''$) uses a non-equilibrium phase change formulation applied in many drying applications [48, 56-58], which are defined in terms of how far vapor concentrations are from the equilibrium condition [48]:

$$\dot{m}_w''' = k_{evap}\left(\frac{M_v}{RT_g}\right)(P_{sat} - P_v) \tag{24}$$

where k_{evap} is the evaporation constant (s^{-1}) that is material and process-dependent, which is given by the reciprocal of the time to reach equilibrium mass transfer [58]. Zanoni et al. [48] observed that the overall impact of k_{evap} on the temperature evolution is small and equilibrium mass transfer is reached for $k_{evap} > 5$ s^{-1}. Eq. 24 shows that evaporation occurs when $P_{sat} > P_v$, while condensation dominates when $P_{sat} < P_v$.

P_{sat} is the saturation vapor pressure presented by [67]:

$$P_{sat} = 610.78\ exp\left(\frac{17.27(T_g - 273.15)}{T_g - 273.15 + 237.3}\right) \tag{25}$$

2.1.3 Energy and Mass Balance

A 1-D global energy balance is applied:

$$\dot{E}_{net} = \dot{E}_{in} + \dot{E}_{evap} + \dot{E}_{oxid} + \dot{E}_{loss} + \dot{E}_{out} \quad (26)$$

where $\dot{E}_{net}$ is the net energy rate stored in porous media, which is the sum of the energy rate from the heater, evaporation, oxidation, system energy loss and energy leaving from the outlet. Each term has been defined in Zanoni et al. [17-19, 23, 48] and is shown in Table SM-1.

Eqs. 27-29 quantify the transient changes of GAC and water mass in the system, which were compared with the experimental measurements to provide confidence in the model:

$$\dot{m}_{GAC} = \int_0^H \rho_{GAC,b} Y_{GAC} A_{cs} dx \quad (27)$$

$$\dot{m}_{water} = \int_0^H \emptyset \rho_w S_w A_{cs} dx \quad (28)$$

$$\dot{m}_{total} = \dot{m}_{GAC} + \dot{m}_{Water} \quad (29)$$

2.2 Experiment

Eight wet smoldering experiments were carried out in a stainless-steel column (Fig. 1) to calibrate the numerical model following the published methodology [55]. Base case (#4) was conducted in quadruplicate along with another four experiments (Cases #1, 7-9) varying the initial water saturations ($S_{w,0}$), Table 1. The smoldering reactor was 0.90 m tall with a 0.108 m inside diameter (Fig. 1), allowing the continuous measurement of axial temperatures and mass loss. The fixed bed contained a 0.73 m wet treatment layer, topped by 0.15 m of the dry clean layer. Both layers used sieved coarse sand (1.19-2.36 mm), while water and oven-dried GAC were mixed with sand to create the wet treatment layer. The GAC and sand properties are detailed in [55]. The wet smoldering experiments started by applying radiative heating at the bottom of the reactor. Then, airflow ($u_{g,in}$) was introduced at t_g to initiate the smoldering when the second TC (TC_2) reached 300 ℃. The airflow was uniformly injected at the bottom of reactor via a set of pipe spargers and the volumetric flow rate (27 L/min) was controlled by a mass flow controller, resulting in a 5 cm/s Darcy velocity. The heater was turned off at t_h (TC_3 peaked) while the air flux was maintained to support the self-sustained smoldering propagation. Table 1 summarizes key experimental conditions and results that were used in the analyses below, and additional details of these experiments are available in Fig. SM-1.

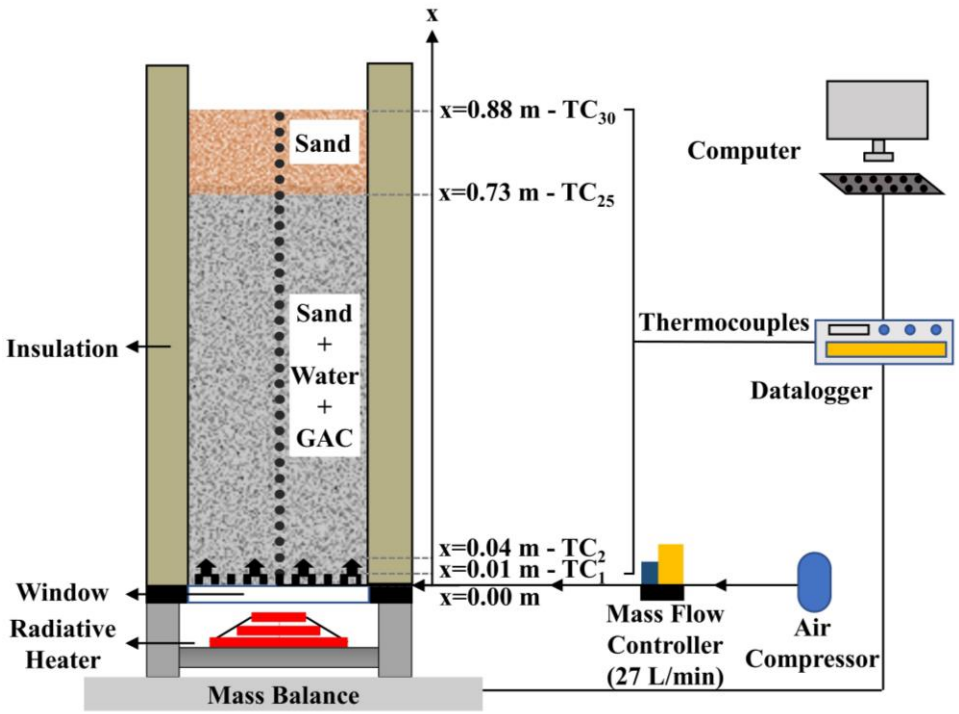

Figure 1: Schematic of the smoldering apparatus.

3 Results and Discussion

3.1 Model Calibration

The model was calibrated to Cases #1, 4, 8-9 by optimizing three empirical coefficients (δ, γ, k_{evap}) via "Pattern Search Algorithm" in MATLAB according to the ranges: δ = 1-10, γ = 0.5-1, and k_{evap} = 0.5-5 s^{-1} until Eq. 23 converged to a minimum value for each case. The optimized parameter values are summarized in Table 1, in which δ and γ have a greater impact on the overall simulation results than k_{evap} as discussed in [48].

Fig. 2 shows the comparison of the temperature evolution between experiments and numerical predictions with different δ and γ, indicating that the calibration process can result in an excellent agreement for the temperature histories with small optimization errors (Table 1). The smoldering time (t) was normalized to compare different $S_{w,0}$ conditions and it is referred to as Dimensionless Time (DT) based on [29]:

$$DT = (t - t_g)\left(\frac{u_s}{L}\right) \tag{30}$$

where $DT = 1$ represents that the smoldering front approaches the end of contaminated pack (0.73 m).

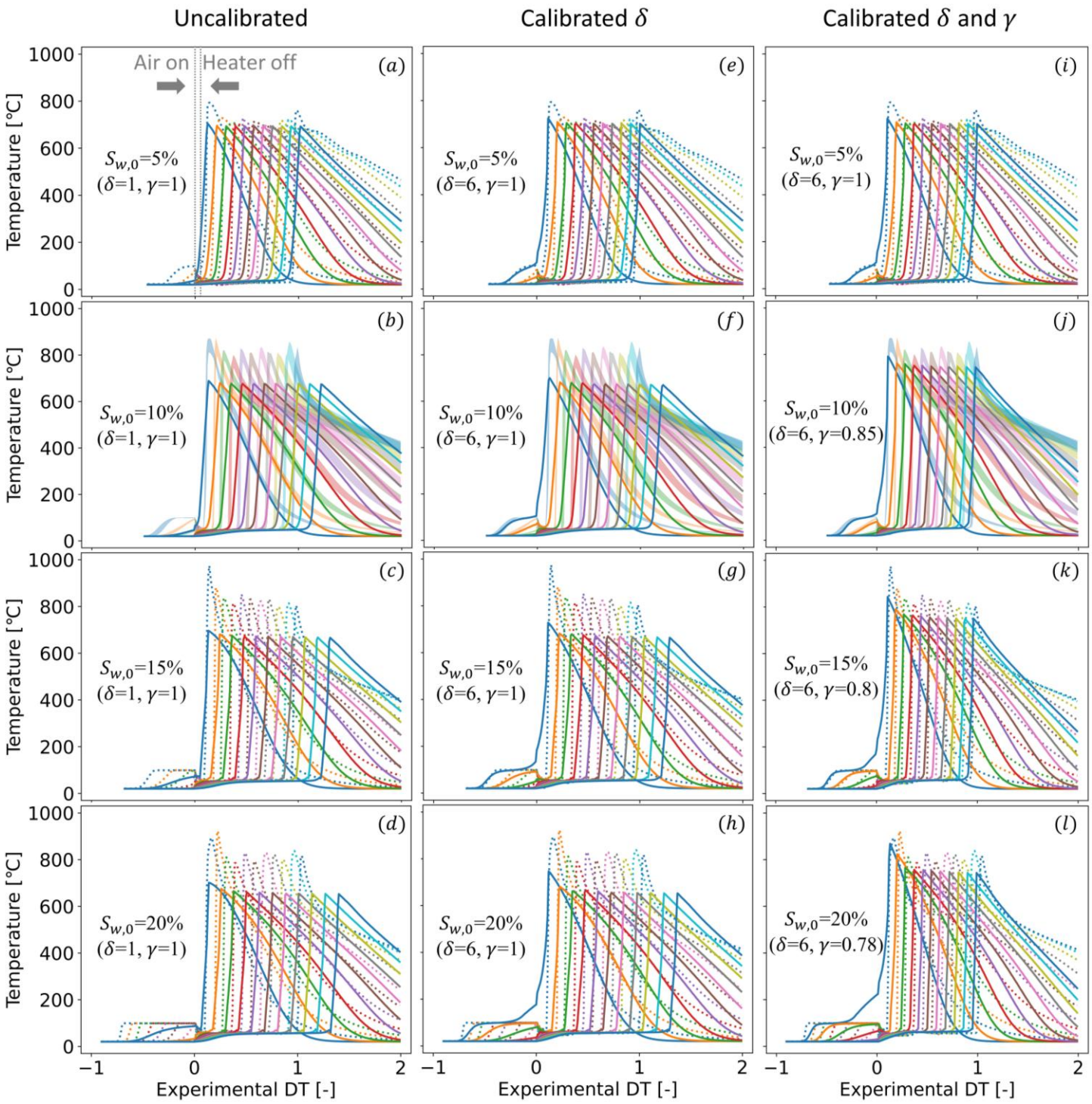

Figure 2: Temperature evolution versus experimental *DT* for Case #1 (a, e, i), #4 (b, f, j), #8 (c, g, k) and #9 (d, h, l). Colours describe TC positions (x) from 0.10 to 0.70 m with 0.06 m intervals. Colored shading shows the range of values associated with four experimental repeats and dashed lines represent single experimental measurement. Solid lines are the

average of the numerical solid (T_s) and gas (T_g) temperatures ($T_{avg} = \frac{T_s+T_g}{2}$) with different calibration constants: a-d (uncalibrated), e-h (calibrated δ), i-l (calibrated δ and γ). Experimental *DT=1* represents the time when smoldering was complete in the experiment, numerical smoldering front beyond *DT=1* means predicted smoldering velocity is slower than the experiments.

Without the calibration of δ and γ (Figs. 2a-d), there is a discrepancy between experimental and predicted temperature profiles in the entire time and space domain, with the increase of initial water saturation ($S_{w,0}$). This observation is in accordance with [48], suggesting that the traditional weighted averaged method of thermal conductivity and specific heat capacity (assuming δ, γ=1 in Eqs. 19-20) cannot accurately simulate heat transfer mechanisms in wet porous media, requiring additional correction constants.

As shown in Figs. 2e-h, optimizing δ could improve the water boiling behavior (i.e., plateau of 100 ℃) at $DT < 0$. It is hypothesized that a high δ is a result of the 2-D impact of the stainless-steel column wall. Stainless-steel has a much higher thermal conductivity (at 25 ℃) than sand (14.7 W m^{-1} K^{-1} versus 0.28 W m^{-1} K^{-1} at 25 ℃), thus the column wall might be heated faster by the bottom heater than the sand mixture. It provides an extra conductive heat transfer to accelerate the water evaporation, which is represented by the improvement of the temperature plateau at 100 ℃ when water is boiling at $DT < 0$ (e.g., Figs 2b, f). However, as δ is mostly related to the conductive heating, its impact on the forward smoldering propagation could be neglected when the convective heating takes place at $DT > 0$ (i.e., air on) as defined in Eq. 19. Besides, the optimized δ was found to be insensitive to the initial water saturation $S_{w,0}$ and had a limit to improve boiling behaviors with the further increase of $S_{w,0}$ (Figs. 2g-h). This behavior is expected as δ is mainly related to the extra heating of the column wall, in which the column material and

heat flux from the heater were fixed in all cases. Note that the 2-D impact might be more obvious in wet smoldering than dry smoldering as water phase change is occurring within a low temperature range (≤ 100 ℃), which is more sensitive to the potential heat transfer in the system.

After optimizing δ and γ together, the ignition stage ($DT < 0$) and smoldering propagation ($DT \geq 0$) were both satisfactorily predicted in each case (Figs. 2i-l) with small errors (Table 1). This improvement is hypothesized to be related to introducing a low γ, which effectively corrects the LTNE between water and sand particles during the water evaporation. As water is assumed to behave as a film coating the sand particles, water film might receive most of the heat first and evaporate into vapor before the sand particles are heated completely. Under this condition, massive water vapor can be produced within a short time, which moves upwards under buoyancy forces ($DT < 0$) and forced airflow ($DT \geq 0$). The vapor will then condense in the cold wet mixture ahead of the smoldering front, releasing a large amount of latent heat and significantly enhancing convective heat transfer. Consequently, γ is empirically acting as the average extent that sand particles are heated uniformly during the overall evaporation process, which decreases with $S_{w,0}$ because the film coating the sand particle is thicker and the heat penetration into the sand particles is slower (see Section 3.2 for more details).

As shown in Fig. 2 (e.g., Figs. 2b, f, j), γ could be used to fix the underestimated heat transfer for both ignition stage and smoldering propagation. Base case (#4), for example, had an average smoldering velocity (u_s) of 0.636 $\pm$ 0.005 cm/min (experimental), and 0.619 cm/min (numerical); the average peak temperature (T_p) were 794 $\pm$ 12 ℃ (experimental) and 761 ℃ (numerical). Refer to Table SM-2 for details of all cases. In contrast to high-temperature peaks in the smoldering front, the 100 ºC boiling plateau during "air off" was replaced by a lower temperature plateau after "air on" both experimentally and numerically at 50 ℃, which the same behavior has been seen in many

wet smoldering studies [e.g., 2, 6, 10, 12]. The low-temperature plateau during "air on" was due to the water condensation ahead of the smoldering front under the forced airflow, named evaporative cooling [48], which was discussed in Section 3.3.2.

It is worth noting the underestimation of the boiling rate observed in Case #9 (Fig. 2l) even after the optimization. It was hypothesized that $S_{w,0} = 20\%$ might be beyond the specific retention of the porous mixture and thus liquid water might drain under the force of gravity and accumulate in the bottom, which was not considered in the model. Liquid mobility was supported by the temperature profile at x = 0.10 m, where the moisture was evaporated slower in the experiment than the prediction (> 100 ºC, Fig. 2l), suggesting a higher water saturation in the bottom of the experimental reactor. Consequently, more water content was close to the heater, absorbing more energy and accelerating the water boiling in the experiment of Case #9. However, both smoldering propagation and evaporation cooling behaviors were predicted well in Case #9, which suggests that liquid mobility might not significantly affect the wet smoldering since airflow on ($DT \geq 0$), providing the confidence to apply the current model to investigate air forced wet smoldering at high $S_{w,0}$ conditions. As liquid mobility is beyond the scope of this model, it will not be simulated in this work.

3.2 Model Extrapolation

The empirical coefficient, γ, related to the thickness of water film, is a function of the initial water saturation, $S_{w,0}$. Fig. 3 shows a γ-$S_{w,0}$ relationship based on the optimized γ and $S_{w,0}$ of Cases #1, 4, 8-9 presented in Table 1. When $S_{w,0}$ is low (< 5%), the porous system is relatively dry and water film is thin so that the impact of water on sand heat transfer is negligible and temperature is uniform inside the sand particles during evaporation (i.e., $\gamma = 1$), similar to the dry smoldering [17, 10-23]. When $S_{w,0}$ is higher (> 5%), γ decreases with $S_{w,0}$ because the heat transfer starts to be affected by the thick water film and rapid water evaporation, resulting in non-uniform heating of sand particles during water evaporation. Nevertheless, the thickness of the water film and evaporation rate might be restricted by the porous system (e.g., grain size) under high $S_{w,0}$ conditions [68], which suggests that γ is limited with further $S_{w,0}$ increases, leading to a power law relationship between γ and $S_{w,0}$:

$$\gamma = 0.56\ (S_{w,0})^{-0.19}\ (\mathrm{S_{w,0}} \geq 5\%) \tag{31}$$

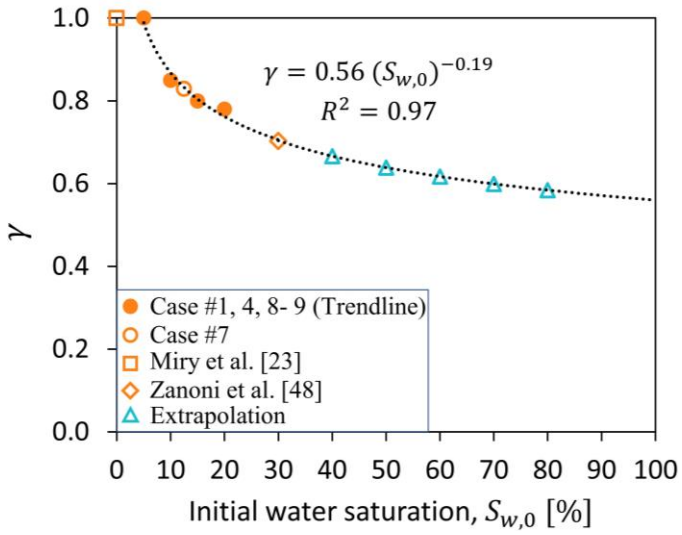

Figure 3: γ-$S_{w,0}$ correlation, developed from optimized Cases #1, 4, 8-9 (four solid orange circles). $\gamma = 1$ in the dry smoldering system (hollow orange square) [23]. The correlation predicts γ (0.829) for Case #7 (hollow orange circle) and γ (0.700) for drying wet porous media at $S_{w,0} = 30\%$ in [48] (hollow orange diamond). Extrapolation of γ-$S_{w,0}$ correlation for Cases #10-23 (hollow blue triangles).

Eq. 31 was then applied to simulate Case #7 ($S_{w,0} = 12.5\%$, Table 1), while δ and k_{evap} were kept constant, without any additional fitting. The predicted temperature evolution shows a good agreement with experimental data with an overall error of 8.51% (Fig. SM-2). In addition, Eq. 31 predicts the same optimized γ found for an air-heated drying process of wet porous media at $S_{w,0} = 30\%$ [48], in which sand used was the same as in this work, although there was no smoldering and the reactor was different. Therefore, this reveals that if the properties of porous media are similar to this study, the developed γ-$S_{w,0}$ correction should be valid for air-heated drying porous media under a range of $S_{w,0}$ s. As for Cases #10-23, γ was determined by extrapolation of Eq. 31 (Table 1), which offered an effective mean to perform the sensitivity analysis of wet smoldering under high $S_{w,0}$ conditions.

3.3 Dynamics: Base case

3.3.1 Mass Balance

The mass loss of GAC and water during wet smoldering can be calculated for Base case (#4) from Eqs. 27-29. A good match was observed between the measured and estimated total mass loss in the system (Fig. 4a), which confirmed that the global mass balance was correctly solved in the model. Fig. 4b shows the predicted temporal GAC and water mass changing with DT, while Fig. 4c plots the corresponding mass loss rate. As expected, the slight mass loss during the ignition stage ($DT < 0$) was mainly attributed by water evaporation. Since the upper part of the column was cold, most of water vapor condensed in that area, resulting in a minor amount of vapor leaving the system. When airflow was injected ($DT \geq 0$), an immediate increase in mass loss rate was observed in both GAC and water. The sufficient oxygen flow supported the self-sustained smoldering propagation, oxidizing and removing GAC at a constant velocity (Fig. 4c). However, similar to the ignition stage, the majority of the reactor was still cold in the beginning, thus, most of the vapor could only condense and accumulate in the porous medium (see discussion in Section 3.3.2). This could be observed via a small increase in water mass loss rate at $DT = 0$ (Fig. 4c) when vapor was slowly leaving the system. As the reaction progressed in time, smoldering front was reaching and heating the upper cold regions; more water accumulated was evaporating and started to leave the system from the top outlet (i.e., gradually increased water mass loss rate in Fig. 4c). Finally, the mass loss rate of water peaked right before smoldering front approached the end of treatment layer. The mass balance proves that the presence of water resulted in a dynamic wet smoldering system that needs to be carefully studied.

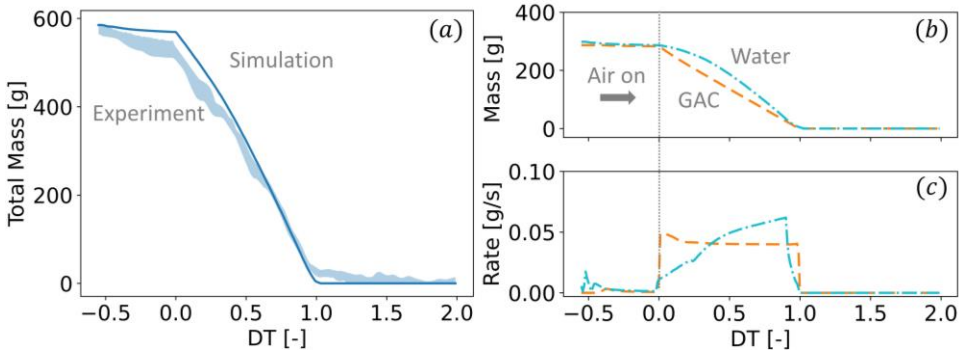

Figure 4: Mass data varying with *DT* for Base Case (#4). (a) Total mass change (water + GAC) measured (colored shading shows four experimental repeats) and predicted (dark blue solid line), (b) predicted mass change and (c) predicted mass loss rate for water (blue dot-dash line) and GAC (orange dash line).

3.3.2 Evaporation, Condensation and Smoldering

Fig. 5 shows the model-predicted variables for Base case (#4). During the ignition stage ($DT < 0$), water evaporation was rapidly initiated near the heater. The produced vapor moved to the upper regions (increasing Y_v at x = 0.10 m in Fig. 5b) due to the pressure-driven convection (slight u_g in Fig. 5d). High Y_v led to the relative humidity (RH) above 100% (Fig. 5f), and thus vapor condensed at x = 0.10 m (negative m_{evap} in Fig. 5e), increasing local water saturation above 20% (Fig. 5c). The significant increase of S_w due to condensation reveals the importance of considering condensation in wet smoldering processes. In addition, the energy released by condensation along with heat transfer mechanisms increased the temperature at x = 0.10 m up to approximately 98.5 ºC simulating the boiling plateau (Fig. 5a). Once the area near the heater was dried (x = 0 m), vapor condensation at x = 0.10 m was terminated and evaporation occurred, resulting in a positive evaporation rate m_{evap} (Fig. 5e). When water is eliminated and evaporation is terminated, heat transfer mechanisms increased the temperature above 100 ℃. Although the region near the heater was effectively evaporating water, the upper regions were relatively cold and vapor could only reach up to 0.22 m and then condensed there (Fig. 5b), confirming only a slight mass loss in the ignition stage (Fig. 4). Further explanation can be found in [48].

When $DT \geq 0$, airflow injection triggered two important processes: GAC smoldering and convective drying (evaporative cooling). The introduction of the air flux ($DT = 0$) enhanced the water evaporation near the heater until complete water removal, and then the increased temperature initiated the self-sustained smoldering in dry and hot regions (e.g., x = 0.10 m in Fig. 5a, temperature > 100 ºC). The successive temperature peaks indicated the self-sustained smoldering propagation was advancing with a constant velocity [50]. In addition, the condensation of water vapor occurred in the upper regions, resulting in negative m_{evap} values above x = 0.22 m and a

temperature plateau around 50 ℃(Figs. 5a, e). This observation proves that the temperature plateau during evaporative cooling is a result of condensation rather than evaporation, which is different from the hypothesis stated by [10]. A lower temperature plateau during evaporative cooling than the boiling stage was due to the forced air flux, which carried the vapor forwards, reducing the high vapor accumulation. This led to less condensation and less energy released to the system [48], therefore, only increasing the temperature up to 50 ℃. Although vapor condensation was relatively small during the evaporative cooling, it cannot be ignored in large reactors or continuous systems since water can easily accumulate (e.g., S_w was increased by 50% at x = 0.70 m in Fig. 5c), which might reach a critical water saturation and lead to extinction [30]. This observation is important as it explains how water dynamically affects the smoldering system (see Video SM-1). At $DT = 1$, when smoldering reached the end of the treatment layer, water and GAC were eliminated without any mass change (Fig. 4).

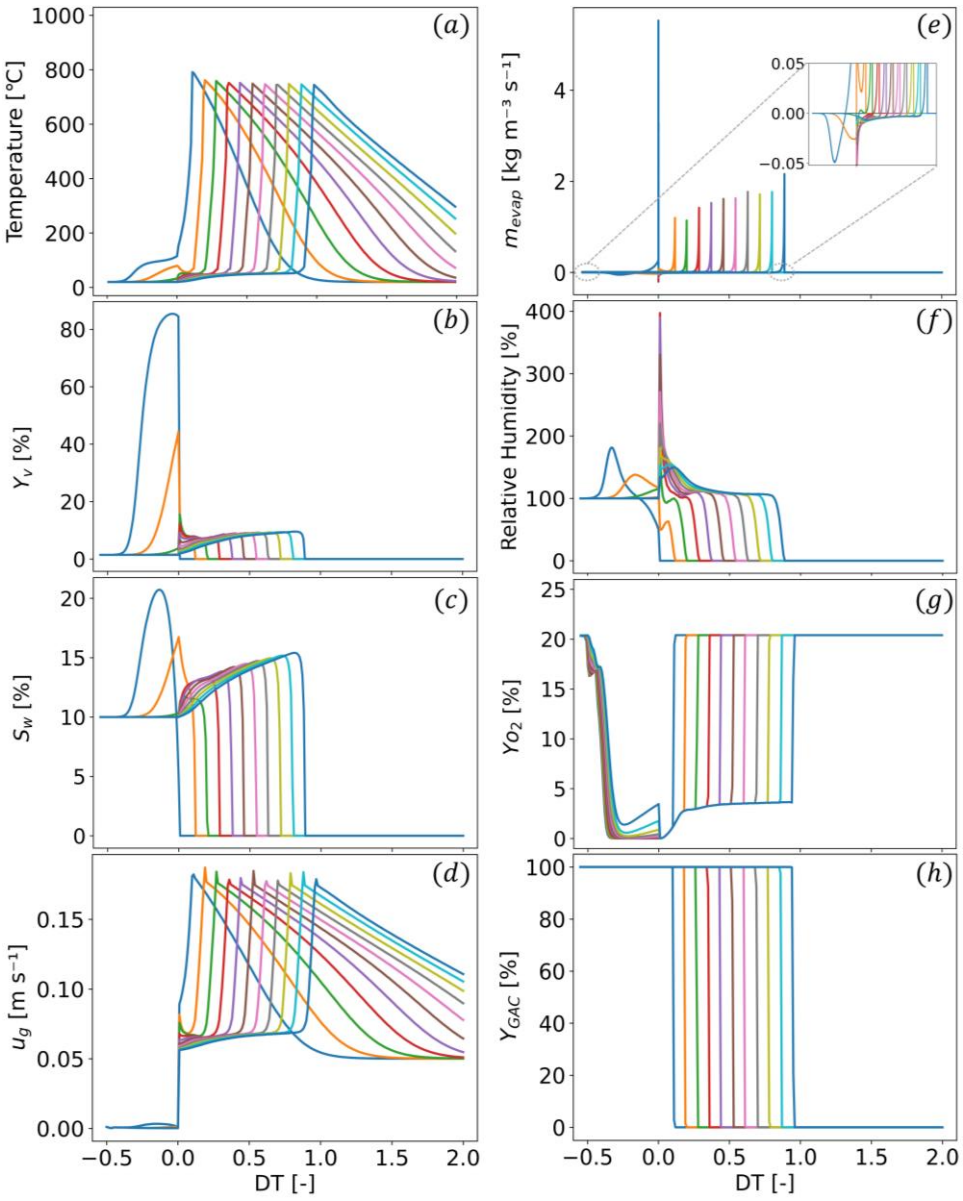

Figure 5: Predicted variables versus *DT* from 0.10 to 0.70 m with 0.06 m intervals for Base case (#4).

3.3.3 Wet Smoldering Front

Fig. 6 shows the wet smoldering front of Base case (#4) divided into five regions at $DT = 0.5$, plotted as a function of column height. The mass fraction of oxygen was normalized as $Y_{O_2,N}$ ($Y_{O_2}/Y_{O_2,0}$) to compare with Y_{GAC}. Region I is the cooling zone, where GAC and water were completely removed ($Y_{GAC} = 0$ & $S_w = 0$), leaving only hot clean sand behind; therefore, oxygen remained at ambient condition. Region II is the smoldering front, where GAC and oxygen were immediately consumed ($0 < Y_{GAC}$ & $Y_{O_2,N} < 1$), and temperature reached the peak. This region was limited to a narrow area, whose thickness (δ_{smol}) was 0.52 cm as shown in Fig. 6. Ahead of smoldering front was the pre-heating front (Region III), where the moisture was completely removed ($Y_{GAC} = 1$ & $S_w = 0$), and temperature started to increase above 100 ℃ after passing the evaporation stage. The pre-heating front served as an important dry buffer between smoldering front and wet regions, protecting smoldering reaction from quenching. Therefore, the thickness of pre-heating front ($\delta_{pre} = 4.09$ cm) is vital for the self-sustained wet smoldering, and is affected by experimental conditions, e.g., $S_{w,0}$, inject airflow and fuel concentration (See discussion in Section 3.4). Region IV is the evaporation front ($\delta_{evap} = 4.82$ cm) where RH was below 100% and liquid water was evaporating ($S_w > 0$ & RH $< 100\%$). However, as shown in Fig. 6, evaporation front had the highest S_w after passing the condensation stage, beyond $S_{w,0}$ (10%), which might cause high hydraulic pressures, suppressing the pre-heating front and affecting smoldering zone. Region V is the condensation front and had RH above 100% (evaporative cooling stage in Fig. 5a, ~ 50 ℃ temperature plateau), resulting in a higher S_w than $S_{w,0}$. In addition, smoldering, evaporation and condensation fronts propagated at a same velocity (~0.619 cm/min in Case #4) after a short period of stabilization time when the system was switched from "air off" to "air on". This suggests that δ_{smol}, δ_{pre} and δ_{evap} were constant, thus the overlapping between

smoldering and evaporation fronts is not likely to happen under self-sustained conditions, as suggested by [47]. Similar behaviors can be seen in other self-sustained cases (not shown).

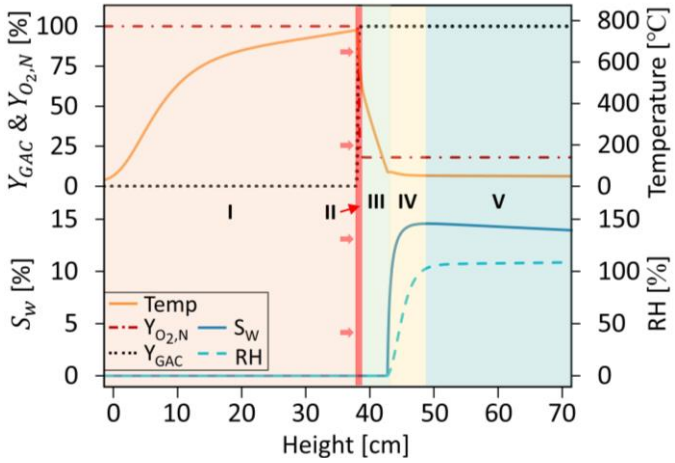

Figure 6: Wet smoldering structure divided into five zones versus height at $DT = 0.5$ for Base case (#4) based on temperature (solid orange line), normalized mass fraction of oxygen (purple dash-dotted line), mass fraction of GAC (black dotted line), local water saturation (dark blue solid line) and relative humidity (blue dashed line). Zone I: cooling, Zone II: smoldering (propagation following red arrows), Zone III: pre-heating, Zone IV: evaporation and Zone V: condensation.

3.4 Sensitivity Analysis

The impact of three key variables on the applied wet smoldering was investigated via numerical modelling at DT = 0.5: initial water saturation, injected airflow and fuel concentration (Fig. 7). Case #17 was not shown in the following comparison as it extinguished near $DT = 0$ (Fig. SM-2).

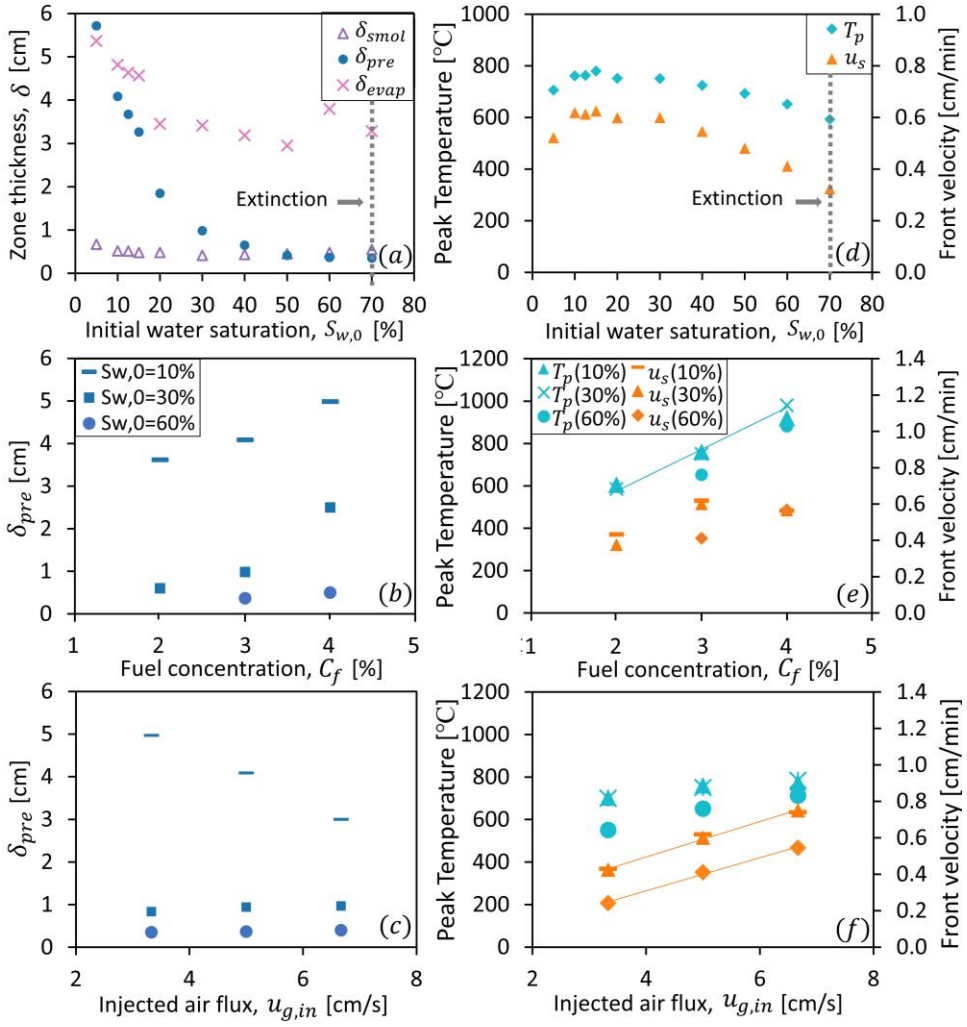

Figure 7: Sensitivity analysis of the impact of initial water saturation, fuel concentration and injected air flux (under three $S_{w,0}$ conditions: 10%, 30%, 60%) on the wet smoldering performance: (a) thickness of smoldering, pre-heating and evaporation zones, (b) (c) thickness of pre-heating zone, (d) (e) (f) smoldering peak temperature and front velocity.

3.4.1 Initial Water Saturation ($S_{w,0}$)

Initial water saturation ($S_{w,0}$) is the most important parameter controlling the applied wet smoldering [10]. As shown in Fig. 7a, the thicknesses of the predicted pre-heating zone (dry buffer, δ_{pre}) and evaporation zone (δ_{evap}) both decreased linearly with $S_{w,0}$ from 5% to 20%, suppressed by the high water saturation in the evaporation and condensation zones (Fig. 6). When $S_{w,0}$ was increased, the heat generated from smoldering cannot evaporate and remove water quickly enough, reducing the pre-heating zone. Nevertheless, smoldering zone was still away from the evaporation zone with δ_{pre} above 2 cm ($S_{w,0} < 20\%$) so that smoldering was protected by the dry buffer and was independent on $S_{w,0}$ (Fig. 7d), which is in accordance with the experimental observation for robust wet smoldering [8-10, 69]. Additionally, the introduction of a small amount of moisture (e.g., $S_{w,0} = 5\%$, 10%) might facilitate the heat transfer in the smoldering system compared to dry smoldering due to the high thermal conductivity of water, leading to a slightly increased u_s and T_p with $S_{w,0}$ ($\leq$ 15%, Fig. 7d). And a slightly thinner δ_{smol} at $S_{w,0} = 15\%$ compared to 5% also suggests a faster smoldering rate of GAC than dry smoldering (Fig. 7a) [70].

At high $S_{w,0}$ conditions ($>$ 20%), δ_{pre} and δ_{evap} gradually reached a plateau where δ_{pre} was 3.5 mm at $S_{w,0}$ of 70%. The δ_{pre} plateau close to zero reveals that the dry buffer between smoldering and evaporation zones was disappearing. Smoldering reaction started to be significantly influenced by high water saturation in the wet region, represented by the decreasing u_s and T_p, and increasing δ_{smol} with $S_{w,0} > 20\%$, until the smoldering reaction could no longer overcome the heat sink of water and then extinguishes. Failures of self-sustained wet smoldering (decreasing T_p) were achieved at $S_{w,0} = 70\%$ (Case #22) and 80% (Case #23). In the latter case, the local water saturation hit ~97% at 40 cm height and the δ_{pre} reached 2 mm before extinction (Fig. 8). These

observations are important to the applied wet smoldering because they have proved two hypotheses in the previous literature: 1) water re-condensation might lead to a critical water saturation quenching the smoldering, which is higher than the initial water saturation (97% > 80%) [30]; 2) the pre-heating zone might disappear at high $S_{w,0}$ conditions, which results in a collapse of the smoldering and evaporation fronts as indicated by Yermán et al. [10], causing weak smoldering conditions to the point of extinction. Once the wet smoldering was non-self-sustained, the smoldering front propagation gradually became slower until it stopped when the system temperature was below the GAC ignition point (300 ℃). However, the remaining heat and forced airflow still sustained the water evaporation and supported the evaporation front moving forward, resulting in a growing pre-heating zone. Consequently, δ_{pre} increased until the evaporation stopped when the system was cooled to the ambient temperature (Fig. 8b).

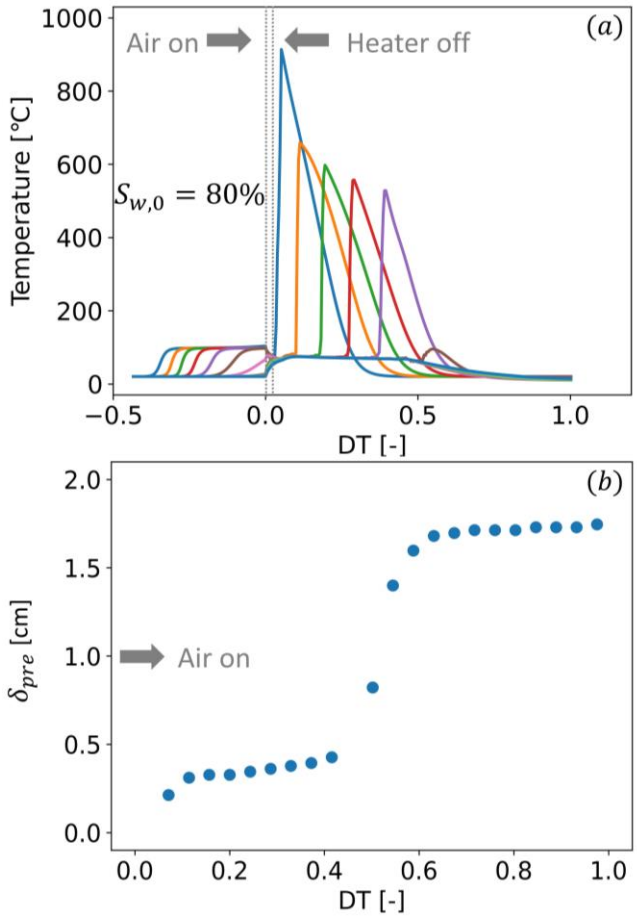

Figure 8: Numerical results of an extinction case at $S_{w,0}$ = 80% (Case #23): (a) predicted temperature evolution versus *DT* from 0.10 to 0.70 m with 0.06 m intervals, (b) predicted development of δ_{pre} since air on ($DT \geq 0$).

Fig. 9 summarizes the global energy balance for each case presented at DT = 0.5, where the energy rate from the heater was not shown as it was off (i.e., $\dot{E}_{in} = 0$) around $DT = 0.1$. Fig. 9a underscores that water is a significant energy sink to the smoldering system, consuming a great amount of energy for evaporation ($\dot{E}_{evap}$) and decreasing $\dot{E}_{net}$; while $\dot{E}_{net} > 0$ is critical for self-sustained smoldering [17].

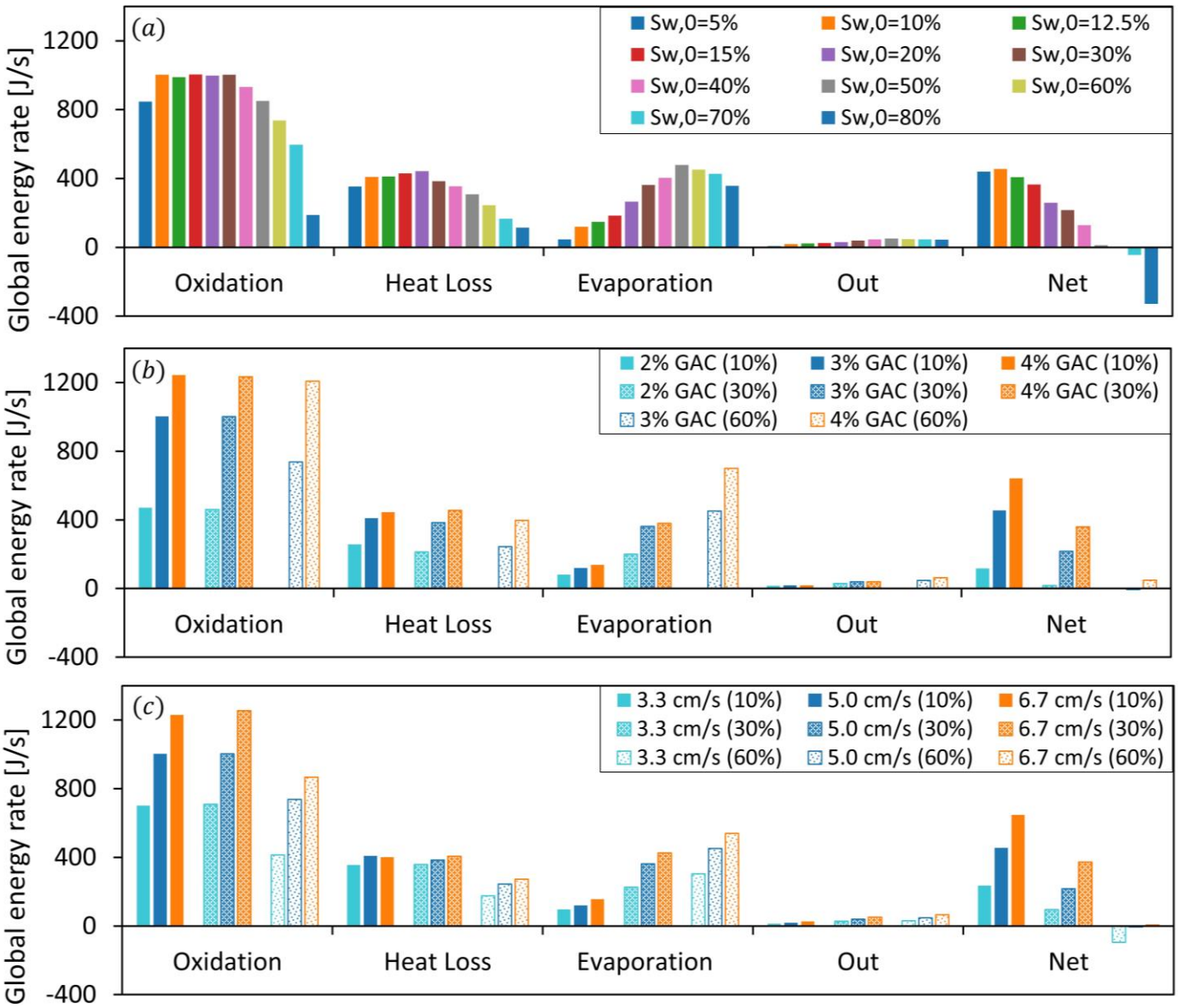

Figure 9: Global energy balance for all cases analyzed *DT* = 0.5 for (a) initial water saturation, (b) fuel concentration under three $S_{w,0}$ conditions (10%, 30%, 60%) and (c) injected air flux under three $S_{w,0}$ conditions (10%, 30%, 60%).

During low $S_{w,0}$ conditions ($\leq$ 20%), the smoldering and evaporation fronts were separated by a dry buffer. Therefore, oxidation was not affected by the presence of water, showing a similar $\dot{E}_{oxid}$. Besides, as $\dot{E}_{loss}$ and $\dot{E}_{out}$ are not impacted by the presence of water [17-19, 21-22], $\dot{E}_{net}$ was solely reduced by $\dot{E}_{evap}$ while remaining well above zero (e.g., 260 J/s at $S_{w,0} = 20\%$), which

explains why the smoldering reaction is independent of $S_{w,0}$. When $S_{w,0}$ is high ($>$ 20%), two factors were starting to negatively affect the smoldering propagation: 1) disappearing dry buffer (i.e., $\delta_{pre} \approx 0$) introduced significant endothermic evaporation into the smoldering zone, which weakened the smoldering reaction, greatly decreasing $\dot{E}_{oxid}$ and T_p (Figs. 7d, 9a); 2) increasing $\dot{E}_{evap}$ with $S_{w,0}$ as more water was evaporating driven by the smoldering reaction (Fig. 9a). Altogether, these led to a low $\dot{E}_{net}$ at $S_{w,0} = 50\%$ (12 J/s), which reached the borderline self-sustained smoldering ($\dot{E}_{net} \approx 0$). $S_{w,0}$ above 50% caused negative $\dot{E}_{net}$ values, in which the global wet smoldering system was losing energy (decreasing T_p) and could no longer sustain itself. Once the smoldering started to quench, $\dot{E}_{oxid}$ decreased immediately while $\dot{E}_{evap}$ reduced gradually supported by the remaining heat and forced airflow.

3.4.2 Fuel Concentration (C_f)

Fuel concentration is a key concern in applied wet smoldering scenarios, which determines how much energy is available to handle the wet conditions. C_f was studied under three $S_{w,0}$ conditions: 10% (low), 30% (medium) and 60% (high). The increase of C_f (from 2% to 4%) accelerated the fuel oxidation, which tripled the GAC oxidation rate (from ~0.45 to 1.25 J/s) and considerably increased the global net energy rate (Fig. 9b). This led to the substantial improvement of T_p in all $S_{w,0}$ conditions as shown in Fig. 7e, representing a linear dependence (R^2 = 0.999), which is in accordance with dry smoldering [18].

Nevertheless, u_s exhibited a non-linear relationship with C_f under low and medium $S_{w,0}$s, which was due to oxidation starvation at high C_f, similar to dry smoldering [18]. Under high $S_{w,0}$ conditions (60%), smoldering reaction was weak at C_f of 3% so that the oxygen was rich. Once C_f was increased, smoldering was enhanced to overcome the water impact, correspondingly improving T_p and u_s (Fig. 7e). Additionally, it was found that Cases #6, 14-21 had a similar T_p and u_s under an identical condition of C_f (4%) and $u_{g,in}$ (5 cm/s). This agrees with Yermán et al. [10] that once the smoldering is stable, its performance is dominated by operating parameters (e.g., C_f, $u_{g,in}$) instead of $S_{w,0}$.

Fig. 7b shows that δ_{pre} gradually increased with C_f from 2% to 3%, followed by a significant increase when C_f increased even further under low and medium $S_{w,0}$ conditions. This behavior might be caused by two factors: 1) enhanced T_p could evaporate water fast and increase δ_{pre}; 2) limited u_s at a high C_f further increased δ_{pre} because smoldering might move slower than the evaporation front during the front stabilization period. The difference in front velocity allowed the expansion of the pre-heating zone, then the velocity difference disappeared after the stabilization

when all the fronts moved forward at the same velocity. Nevertheless, the impact of u_s on δ_{pre} was mitigated under high $S_{w,0}$ conditions, in which the evaporation front propagation is strictly driven by the smoldering front.

3.4.3 Air Flux ($u_{g,in}$)

Injected airflow is one of the most practical ways to control applied wet smoldering behaviors. Fig. 7f shows that both T_p and u_s increased with $u_{g,in}$ from 3.3 to 6.7 cm/s due to the enhancement of the global oxidation rate and net energy rate in all $S_{w,0}$ conditions (Fig. 9c). u_s represents a linear positive relationship with $u_{g,in}$ ($R^2 = 0.999$), while a weaker sensitivity of T_p to $u_{g,in}$ was observed, similar to dry smoldering [18].

δ_{pre} was found to decrease with $u_{g,in}$ at low $S_{w,0}$ (10%), which was against intuition as $\dot{E}_{net}$ increased and wet smoldering was more stable. This might be related to the increase of u_s since the temperature was not altered much. As discussed in Section 3.4.2, u_s has an impact on δ_{pre}. Increasing u_s might result in faster propagation of the smoldering front than evaporation front during the front stabilization period, reducing δ_{pre}. As the impact of u_s is negligible with further $S_{w,0}$ increases, the decrease of δ_{pre} due to $u_{g,in}$ did not occur under medium and high $S_{w,0}$ conditions, where δ_{pre} was small and mainly controlled by $S_{w,0}$. The above observation suggests that once δ_{pre} is thick enough to separate the smoldering and evaporation fronts (e.g., > 1 cm), δ_{pre} is independent of $\dot{E}_{net}$ while is dominated by the operating parameters, C_f and $u_{g,in}$.

3.5 Extinction Criterion

Fig. 10 plots the global net energy rate versus its corresponding δ_{pre} for all cases presented in Table 1 (except Case #17), which provides a single, graphical summary of many of the points discussed above. The figure underscores that all smoldering extinction cases (Cases #18, 22, 23) exhibit a negative $\dot{E}_{net}$. Borderline self-sustained smoldering case (Cases #16, 19) shows a $\dot{E}_{net}$ close to zero, while self-sustained cases have positive values (refer to Fig. SM-2 for all predicted temperature profiles). For the latter, the magnitude of $\dot{E}_{net}$ represents the robustness of wet smoldering [17-18].

Fig. 10 clearly shows the close relationship between the thickness of pre-heating zone and global net energy rate. When the pre-heating zone was wide ($\delta_{pre} > 1$ cm), the smoldering front was separated from the evaporation front, therefore the smoldering propagation was independent of $S_{w,0}$. In this situation, δ_{pre} was greatly affected by operating processes (e.g., C_f, $u_{g,in}$) and not correlated with $\dot{E}_{net}$. Nevertheless, once the pre-heating zone was thin ($\delta_{pre} \leq 1$ cm), smoldering front started to be suppressed by $S_{w,0}$. δ_{pre} solely depended on the energy balance and showed a strong positive correlation with $\dot{E}_{net}$. Besides, a minimum δ_{pre} was necessary to create a positive $\dot{E}_{net}$ for self-sustained smoldering, which was 4 mm in this work.

Although the global energy balance could predict that extinction will occur, it cannot establish when and where the wet smoldering reaction would quench nor if all the fuel was consumed for such cases [18]. For example, Case #22 is categorized as a non-self-sustained smoldering, exhibiting a negative $\dot{E}_{net}$ (-44 J/) and a thin δ_{pre} (3.5 mm) at $DT = 0.5$. In this case, the smoldering front still can propagate long enough until the end of the contaminated pack with a high T_p above 550 ℃, oxidating all the GAC before the reaction was quenched. This emphasizes

the high energy efficiency of the applied forward smoldering systems, where the energy stored in the cooling zone could continue to support the smoldering propagation for a finite period even though the global net energy rate reached negative [18].

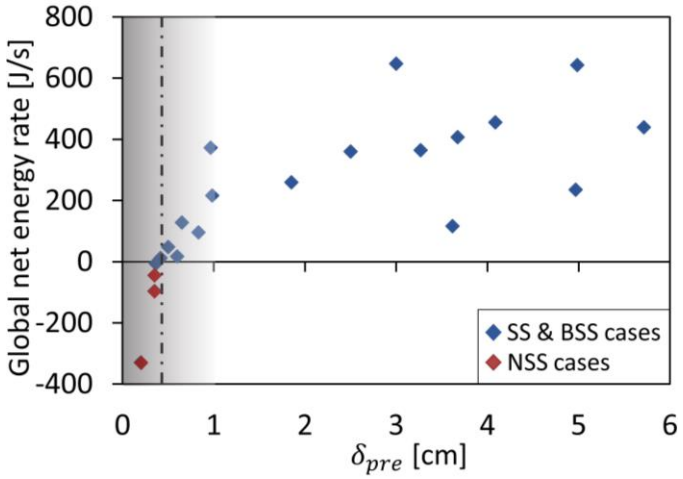

Figure 10: Global net energy rate versus the thickness of preheating zone at $DT = 0.5$.

4 Conclusions

In this work, a numerical model was developed to predict the transient and spatial resolution of the progression of evaporation, condensation, and smoldering fronts in porous media. The comparison between the numerical and experimental results indicated that by introducing simple calibration constants, the model could accurately describe the complex heat and mass transfer mechanisms controlling wet smoldering propagation. Furthermore, the model uncovered the characteristic structure of the wet smoldering front, where the water accumulation in the condensation zone (temperature plateau around 50 ℃) might cause a much higher S_w than the initial condition, posing the risk of smoldering extinction. And wet smoldering could be improved by increasing the fuel concentration and airflow to avoid extinction, which could substantially enhance the global net energy rate. Finally, δ_{pre} and $\dot{E}_{net}$ were found to be closely correlated when the wet smoldering system was affected by high $S_{w,0}$s and δ_{pre} is small (< 1 cm), where a minimum δ_{pre} is required to achieve a positive $\dot{E}_{net}$, preventing extinction.

Overall, this work provides unique insights into the important role of water phase change in the smoldering system, which help engineers better manage the smoldering applications under wet conditions (e.g., treating HMWs). Further study is required to understand other factors affecting smoldering such as influence of pyrolysis products reactions, reactive porous media, high saturation conditions, and liquid movement in porous media.

5 Acknowledgments

Funding was provided by the Natural Sciences and Engineering Research Council of Canada. The in-kind support of Savron is appreciated as well as numerical and laboratory support from RESTORE research group members, especially Dr. Tarek Rashwan, Dr. Christopher Power, Zia Miry, Angelos Almpanis, Joshua Brown, Dr. Taryn Fournie, Shuyang Wang, Huiyi Yang.

This paper is dedicated in loving memory of my supervisor, mentor, and dear friend, Prof. Jason Gerhard.

6 References

[1] J.L. Torero, J.I. Gerhard, M.F. Martins, M.A.B. Zanoni, T.L. Rashwan, J.K. Brown, Processes defining smouldering combustion: integrated review and synthesis, Prog. Energy Combust. Sci. 81 (2020) 100869.

[2] T.L. Rashwan, J.I. Gerhard, G.P. Grant, Application of self-sustaining smouldering combustion for the destruction of wastewater biosolids, Waste Manage. 50 (2016) 201-212.

[3] T.L. Rashwan, T. Fournie, J.L. Torero, G.P. Grant, J.I. Gerhard, Scaling up self-sustained smouldering of sewage sludge for waste-to-energy, Waste Manage. 135 (2021) 298-308.

[4] C. Feng, J. Huang, C. Yang, C. Li, X. Luo, X. Gao, Y. Qiao, Smouldering combustion of sewage sludge: Volumetric scale-up, product characterization, and economic analysis, Fuel 305 (2021) 121485.

[5] C. Feng, M. Cheng, X. Gao, Y. Qiao, M. Xu, Occurrence forms and leachability of inorganic species in ash residues from self-sustaining smouldering combustion of sewage sludge, Proc. Combust. Inst. 38 (2021) 4327-4334.

[6] T.L. Rashwan, T. Fournie, M. Green, A.L. Duchesne, J.K. Brown, G.P. Grant, J.L. Torero, J.I. Gerhard, Applied smouldering for co-waste management: Benefits and trade-offs. Fuel Process. Technol. 240 (2023) 107542.

[7] L. Yermán, R.M. Hadden, J. Carrascal, I. Fabris, D. Cormier, J.L. Torero, J.I. Gerhard, M. Krajcovic, P. Pironi, Y.-L. Cheng, Smouldering combustion as a treatment technology for faeces: exploring the parameter space, Fuel 147 (2015) 108-116.

[8] L. Yermán, H. Wall, J.L. Torero, J.I. Gerhard, Y.-L. Cheng, Smoldering combustion as a treatment technology for feces: Sensitivity to key parameters, Combust. Sci. Technol. 188 (2016) 968-981.

[9] L. Yermán, D. Cormier, I. Fabris, J. Carrascal, J.L. Torero, J.I. Gerhard, Y.-L. Cheng, Potential bio-oil production from smouldering combustion of faeces, Waste Biomass Valorization 8 (2016) 329-338.

[10] L. Yermán, H. Wall, J.L. Torero, Experimental investigation on the destruction rates of organic waste with high moisture content by means of self-sustained smoldering combustion, Proc. Combust. Inst. 36 (2017) 4419- 4426.

[11] A. Serrano, H. Wyn, L. Dupont, D.K. Villa-Gomez, L. Yermán, Self-sustaining treatment as a novel alternative for the stabilization of anaerobic digestate, J. Environ. Manage 264 (2020) 110544.

[12] Z. Song, T. He, M. Li, D. Wu, F. You, Self-sustaining smoldering as a novel disposal approach for food waste with high moisture content, Fuel Process. Technol. 228 (2022) 107144.

[13] C. Zhao, Y. Li, Z. Gan, M. Nie, Method of smoldering combustion for refinery oil sludge treatment, J. Hazard. Mater. 409 (2021) 124995.

[14] Z. Gan, C. Zhao, Y. Li, G. Chen, Z. Song, Z. Zhang, W. Ran, Experimental investigation on smoldering combustion for oil sludge treatment: Influence of key parameters and product analysis, Fuel, 316 (2022) 123354.

[15] T.J. Ohlemiller, Modeling of smoldering combustion propagation, Prog. Energy Combust. Sci. 11 (1985) 227-310.

[16] M.A.B. Zanoni, J.L. Torero, J.I. Gerhard, The role of local thermal non-equilibrium in modelling smouldering combustion of organic liquids, Proc. Combust. Inst. 37 (2019) 3109-3117.

[17] M.A.B. Zanoni, J.L. Torero, J.I. Gerhard, Determining the conditions that lead to self-sustained smouldering combustion by means of numerical modelling, Proc. Combust. Inst. 37 (2019) 4043-4051.

[18] M.A.B. Zanoni, J.L. Torero, J.I. Gerhard, Delineating and explaining the limits of self-sustained smouldering combustion, Combust. Flame 201 (2019) 78-92.

[19] M.A.B. Zanoni, J.L. Torero, J.I. Gerhard, Experimental and numerical investigation of weak, self-sustained conditions in engineered smouldering combustion, Combust. Flame 222 (2020) 27-35.

[20] M.A.B. Zanoni, J. Wang, J.I. Gerhard, Understanding pressure changes in smouldering thermal porous media reactors, J. Chem. Eng. 412 (2021) 128642.

[21] T.L. Rashwan, J.L. Torero, J.I. Gerhard, Heat losses in applied smouldering systems: sensitivity analysis via analytical modelling, Int. J. Heat Mass Transf. 172 (2021) 121150.

[22] T.L. Rashwan, J.L. Torero, J.I. Gerhard, Heat losses in a smouldering system: the key role of non-uniform air flux, Combust. Flame 227 (2021) 309-321.

[23] S.Z. Miry, M.A.B. Zanoni, T.L. Rashwan, J.L. Torero, J.I. Gerhard, Investigation of multi-dimensional transfer effects in applied smouldering systems: A 2D numerical modelling approach, Combust. Flame 246 (2022) 112385.

[24] R. Pan, G. Debenest, M.A.B. Zanoni, A robust two-dimensional model for the pyrolysis of plastic waste driven by self-sustaining smoldering, Process Saf. Environ. Prot. 162 (2022) 610-619.

[25] R. Pan, G. Debenest, M.A.B. Zanoni, Numerical study of plastic waste pyrolysis driven by Char Smoldering, Process Saf. Environ. Prot. 165 (2022) 46-56.

[26] T.L. Rashwan, Self-Sustaining Smouldering Combustion as a Novel Disposal Destruction Method for Waste Water Biosolids, MESc thesis, The University of Western Ontario, London, Canada, 2015.

[27] G. Rein, N. Cleaver, C. Ashton, P. Pironi, J.L. Torero, The severity of smouldering peat fires and damage to the Forest Soil, CATENA 74 (2008) 304-309.

[28] N. Prat-Guitart, G. Rein, R.M. Hadden, C.M. Belcher, J.M. Yearsley, Propagation probability and spread rates of self-sustained smouldering fires under controlled moisture content and bulk density conditions, Int. J. Wildland Fire 25 (2016) 456.

[29] L. Kinsman, J.L. Torero, J.I. Gerhard, Organic Liquid Mobility induced by smoldering remediation, J. Hazard. Mater. 325 (2017) 101-112.

[30] T.L. Rashwan, Sustainable Smouldering for Waste-to-Energy: Scale, Heat Losses, and Energy Efficiency, Ph.D thesis, The University of Western Ontario, London, Canada, 2020.

[31] X. Huang, G. Rein, Downward spread of smouldering peat fire: The role of moisture, density and oxygen supply, Int. J. Wildland Fire 26 (2017) 907.

[32] X. Huang, G. Rein, Smouldering combustion of peat in wildfires: inverse modelling of the drying and the thermal and oxidative decomposition kinetics, Combust. Flame 161 (2014) 1633-1644.

[33] X. Huang, G. Rein, H. Chen, Computational smoldering combustion: predicting the roles of moisture and inert contents in peat wildfires, Proc. Combust. Inst. 35 (2015) 2673-2681.

[34] X. Huang, G. Rein, Computational study of critical moisture and depth of burn in peat fires, Int. J. Wildland Fire 24 (2015) 798-808.

[35] X. Huang, G. Rein, Interactions of Earth's atmospheric oxygen and fuel moisture in smouldering wildfires, Sci. Total Environ. 572 (2016) 1440-1446.

[36] X. Huang, F. Restuccia, M. Gramola, G. Rein, Experimental study of the formation and collapse of an overhang in the lateral spread of smouldering peat fires, Combust. Flame 168 (2016) 393-402.

[37] Y. Hu, E.G. Christensen, H.M.F. Amin, T.E.L. Smith, G. Rein, Experimental study of moisture content effects on the transient gas and particle emissions from peat fires, Combust. Flame 209 (2019) 408-417.

[38] T.C. Mulky, K.E. Niemeyer, Computational study of the effects of density, fuel content, and moisture content on smoldering propagation of cellulose and hemicellulose mixtures, Proc. Combust. Inst. 37 (2019) 4091-4098.

[39] Z. Song, Modelling oxygen-limited and self-sustained smoldering propagation: Underground coal fires driven by thermal buoyancy, Combust. Flame 245 (2022) 112382.

[40] C. Switzer, P. Pironi, J.I. Gerhard, G. Rein, J.L. Torero, Self-sustaining smoldering combustion: a novel remediation process for non-aqueous-phase liquids in porous media, Environ. Sci. Technol. 43 (2009) 5871-5877.

[41] A.L. Duchesne, J.K. Brown, D.J. Patch, D. Major, K.P. Weber, J.I. Gerhard, Remediation of PFAS-contaminated soil and granular activated carbon by smoldering combustion, Environ. Sci. Technol. 54 (2020) 12631-12640.

[42] T. Fournie, C. Switzer, J.I. Gerhard, USEPA LEAF methods for characterizing phosphorus and potentially toxic elements in raw and thermally treated sewage sludge, Chemosphere 275 (2021) 130081.

[43] T. Fournie, T.L. Rashwan, C. Switzer, G.P. Grant, J.I. Gerhard, Exploring PCDD/fs and potentially toxic elements in sewage sludge during smouldering treatment, J. Environ. Manage. 317 (2022) 115384.

[44] T. Fournie, T.L. Rashwan, C. Switzer, J.I. Gerhard, Phosphorus recovery and reuse potential from smouldered sewage sludge ash, Waste Manag. 137 (2022) 241-252.

[45] R.B. Morales, C.T. DeGroot, G.C. Scholes, J.I. Gerhard, Understanding, controlling and optimising the cooling of waste thermal treatment beds including starx hottpads, Waste Manag. Res. 40 (2022).

[46] T.L. Rashwan, J.L. Torero, J.I. Gerhard, The improved energy efficiency of applied smouldering systems with increasing scale, Int. J. Heat Mass Transf. 177 (2021) 121548.

[47] J. Bruining, A.A. Mailybaev, D. Marchesin, Filtration Combustion in Wet Porous Medium, SIAM J Appl Math. 70 (2009) 1157-1177.

[48] M.A.B. Zanoni, J. Wang, J.L. Torero, J.I. Gerhard, Multiphase modelling of water evaporation and condensation in an air-heated porous medium, Appl. Therm. Eng. 212 (2022) 118516.

[49] Y. Dong, J.S. McCartney, N. Lu, Critical review of thermal conductivity models for unsaturated soils, Geotech. Geol. Eng. 33 (2015) 207–221.

[50] K.M. Smits, T. Sakaki, A. Limsuwat, T.H. Illangasekare, Thermal conductivity of sands under varying moisture and porosity in drainage–wetting cycles, Vadose Zone J. 9 (2010) 172–180.

[51] T.T. Lie, Fire and buildings, Appl. Sci. (1972) London.

[52] V.K. Kodur, M.A. Sultan, Effect of temperature on thermal properties of high-strength concrete, J. Mater. Civ. Eng. 15 (2003) 101–107.

[53] Y. Hu, Z. Wang, X. Cheng, C. Ma, Non-isothermal TGA study on the combustion reaction kinetics and mechanism of low-rank coal char, RSC Adv. 8 (2018) 22909–22916.

[54] B.A. Akash, W.S. O'Brien, The production of activated carbon from a bituminous coal, Int. J. Energy Res. 20 (1996) 913–922.

[55] J. Wang, G.P. Grant, J.I. Gerhard, The influence of porous media heterogeneity on smouldering remediation, J. Contam. Hydrol. 237 (2021) 103756.

[56] A. Halder, A. Dhall, A.K. Datta, Modeling Transport in Porous Media With Phase Change: Applications to Food Processing, J. Heat Transf. 133 (2010).

[57] F.A. Khan, C. Fischer, A.G. Straatman, Numerical model for non-equilibrium heat and mass exchange in conjugate fluid/solid/porous domains with application to evaporative cooling and drying, Int. J. Heat Mass Transf. 80 (2015) 513-528.

[58] C. Kumar, M.U.H. Joardder, T.W. Farrell, G.J. Millar, A. Karim, A porous media transport model for apple drying, Biosyst. Eng. 176 (2018) 12-25.

[59] R.E. Sonntag, C. Borgnakke, G.J. Van Wylen, Fundamentals of Thermodynamics, Wiley, U.S., 2002.

[60] M.A.B. Zanoni, J.L. Torero, J.I. Gerhard, Determination of the interfacial heat transfer coefficient between forced air and sand at Reynold's numbers relevant to smouldering combustion, Int. J. Heat Mass Transf. 114 (2017) 90-104.

[61] D.A. Tzempelikos, D. Mitrakos, A.P. Vouros, A.V. Bardakas, A.E. Filios, D. P. Margaris, Numerical modeling of heat and mass transfer during convective drying of cylindrical quince slices, J. Food Eng. 156 (2015) 10-21.

[62] T. Arkhangelskaya, K. Lukyashchenko, Estimating soil thermal diffusivity at different water contents from easily available data on soil texture, bulk density, and organic carbon content, Biosyst. Eng. 168 (2018) 83-95.

[63] U. Kleinhans, S. Halama, H. Spliethoff, The role of gasification reactions during pulverized solid fuel combustion: A detailed char combustion model based on measurements of char structure and kinetics for coal and pre-treated biomass, Combust. Flame 184 (2017) 117-135.

[64] F.P. Incropera, Fundamentals of heat and mass transfer, John Wiley & Sons, U.S., 2007.

[65] J. Aprajeeta, R. Gopirajah, C. Anandharamakrishnan, Shrinkage and porosity effects on heat and mass transfer during potato drying, J. Food Eng.144 (2015) 119-128.

[66] J.L. Torero, A.C. Fernandez-Pello, M. Kitano, Opposed Forced Flow Smoldering of Polyurethane Foam, Combust. Sci. Technol. 91 (1993) 95-117.

[67] A.L. Buck, New Equations for Computing Vapor Pressure and Enhancement Factor, J. Appl. Meteorol. Climatol. 20 (1981) 1527-1532.

[68] R. Marynowski, Experimental Investigations on Evaporation from Porous Media, Ph.D. thesis, University of Windsor, Windsor, Ontario, Canada, 2016.

[69] F. He, W. Yi, Y. Li, J. Zha, B. Luo, Effects of fuel properties on the natural downward smoldering of piled biomass powder: Experimental investigation, Biomass Bioenergy 67 (2014) 288-296.

[70] F.L. Bittencourt, G. Debenest, M.F. Martins, Free convection development caused by bed shrinkage in a vacuum-induced smoldering reactor, J. Chem. Eng. 430 (2022) 132847.